

ACCEPTED MANUSCRIPT

Analysis of an open source, closed-loop, realtime system for hippocampal sharp-wave ripple disruption

To cite this article before publication: Shayok Dutta *et al* 2018 *J. Neural Eng.* in press <https://doi.org/10.1088/1741-2552/aae90e>

Manuscript version: Accepted Manuscript

Accepted Manuscript is "the version of the article accepted for publication including all changes made as a result of the peer review process, and which may also include the addition to the article by IOP Publishing of a header, an article ID, a cover sheet and/or an 'Accepted Manuscript' watermark, but excluding any other editing, typesetting or other changes made by IOP Publishing and/or its licensors"

This Accepted Manuscript is © 2018 IOP Publishing Ltd.

During the embargo period (the 12 month period from the publication of the Version of Record of this article), the Accepted Manuscript is fully protected by copyright and cannot be reused or reposted elsewhere.

As the Version of Record of this article is going to be / has been published on a subscription basis, this Accepted Manuscript is available for reuse under a CC BY-NC-ND 3.0 licence after the 12 month embargo period.

After the embargo period, everyone is permitted to use copy and redistribute this article for non-commercial purposes only, provided that they adhere to all the terms of the licence <https://creativecommons.org/licenses/by-nc-nd/3.0>

Although reasonable endeavours have been taken to obtain all necessary permissions from third parties to include their copyrighted content within this article, their full citation and copyright line may not be present in this Accepted Manuscript version. Before using any content from this article, please refer to the Version of Record on IOPscience once published for full citation and copyright details, as permissions will likely be required. All third party content is fully copyright protected, unless specifically stated otherwise in the figure caption in the Version of Record.

View the [article online](#) for updates and enhancements.

1
2
3
4
5
6
7
8
9
10
11
12
13
14
15
16
17
18
19
20
21
22
23
24
25
26
27
28
29
30
31
32
33
34
35
36
37
38
39
40
41
42
43
44
45
46
47
48
49
50
51
52
53
54
55
56
57
58
59
60

Analysis of an open-source, closed-loop, realtime system for hippocampal sharp-wave ripple disruption

Shayok Dutta¹, Etienne Ackermann¹, Caleb Kemere¹

¹Department of Electrical and Computer Engineering, Rice University, Houston, Texas

E-mail: {caleb.kemere}@rice.edu

Abstract.

Objective. The ability to modulate neural activity in a closed-loop fashion enables causal tests of hypotheses which link dynamically-changing neural circuits to specific behavioral functions. One such dynamically-changing neural circuit is the hippocampus, in which momentary sharp-wave ripple (SWR) events — ≈ 100 ms periods of large 150–250 Hz oscillations — have been linked to specific mnemonic functions via selective closed-loop perturbation. The limited duration of SWR means that the latency in systems used for closed-loop interaction is of significant consequence compared to other longer-lasting circuit states. While closed-loop SWR perturbation is becoming more wide-spread, the performance trade-offs involved in building a SWR disruption system have not been explored, limiting the design and interpretation of paradigms involving ripple disruption. *Approach.* We developed and evaluated a low-latency closed-loop SWR detection system implemented as a module to an open-source neural data acquisition software suite capable of interfacing with two separate data acquisition hardware platforms. We first use synthetic data to explore the parameter space of our detection algorithm, then proceed to quantify the realtime *in vivo* performance and limitations of our system. *Main results.* We evaluate the realtime system performance of two data acquisition platforms, one using USB and one using ethernet for communication. We report that signal detection latency decomposes into a data acquisition component of 7.5–13.8 ms and 1.35–2.6 ms for USB and ethernet hardware respectively, and an algorithmic component which varies depending on the threshold parameter. Using ethernet acquisition hardware, we report that an algorithmic latency in the range of ≈ 20 –66 ms can be achieved while maintaining < 10 false detections per minute, and that these values are highly dependent upon algorithmic parameter space trade-offs. *Significance.* By characterizing this system in detail, we establish a framework for analyzing other closed-loop neural interfacing systems. Thus, we anticipate this modular, open-source, realtime system will facilitate a wide range of carefully-designed causal closed-loop experiments.

1. Introduction

Historically, precisely-targeted lesion studies have been the gold-standard to establish causal relationships between neural regions and cognitive functions, for example, studies showing hippocampal involvement in recognition and Pavlovian contextual fear memories [1, 2]. Modern tools such as opto- and chemo-genetics enable these perturbations to have reversible effects and to be targeted to specific genetically-specified cells. However, for many neural circuits, emerging hypotheses link specific functions to specific patterns of activity or modes of representing information which are present in distinct, temporally-limited periods. Causal tests of these hypotheses require the ability to interact with the brain in closed-loop—detecting and perturbing neural activity only in the desired moments. In some cases, the patterns of interest are brief “ensemble events” having only sub-second duration. Thus, in order to modulate information contained in these patterns, they must be detected not only with high accuracy but also low latency.

Closed-loop systems for detecting and perturbing temporally-distinct patterns of neural activity obligatorily combine both algorithmic (i.e., software) and computational hardware components. There is often a naive assumption that accuracy can be maximized and latency minimized via computational or hardware improvements. However, in many regimes, it is possible that algorithmic trade-offs may be the primary factors constraining detection latency and accuracy. Without a system-level analysis, however, these trade-offs may remain poorly-understood and investigators lose the opportunity to balance performance against potential side-effects of neuromodulation such as seizures, tissue damage, or the induction long-term plasticity. There are three primary challenges to system-level analyses. First, closed-source data acquisition platforms limit the ability to understand or explore the full data processing pipeline. Second, parameter explorations during on-going *in vivo* experiments are limited by the finite nature of neural implants and animal cooperation. Finally, the properties of neural signals are resistant to classical detection theories that rely on well-differentiated “signal” and “noise”.

We present an open-source system we developed to detect sharp-wave ripples (SWRs)—brief periods of elevated 150-250 Hz oscillation in the local field potential (LFP) which are prominent in area CA1 of the hippocampus—and trigger perturbations of ongoing activity (e.g., silencing activity via optogenetic stimulation to hippocampal area CA3 or electrical stimulation of the ventral hippocampal commissural fibers). Such systems have recently been developed and used to investigate the causal significance of neural activity during SWRs in learning, consolidation, and working memory [3–8]. In order to investigate our realtime system, we explored algorithmic parameter spaces by employing a two-level strategy. First, we developed a simulation model of the system allowing us to rapidly and efficiently prototype algorithms and evaluate performance. Second, we built an apparatus to feed pre-recorded neural activity back into our data acquisition system and ran pseudo-experiments with varied parameters. We

applied this strategy to both a synthetic ripple dataset and to data recorded *in vivo* from hippocampal area CA1. After identifying key performance metrics, we show how varying parameters affects system performance using an initial single-channel detection algorithm. We demonstrate how these performance trade-offs depend on both algorithmic choices and system hardware. Finally, we show how enhancing the algorithm to use multiple detection channels can improve system performance at a cost of only minimally increasing processing load and latency.

2. Methods

2.1. Animal Use

For the *in vivo* portion of our study, one male Long Evans rat (Charles River Laboratories) was implanted with a micro-drive array with independently adjustable tetrodes (implant coordinates -3.66 mm AP and 2.4 mm ML relative to bregma). Tetrodes were lowered into hippocampal CA1 over one week. Tetrode locations were determined by characteristic LFP waveforms attributed to the target area in conjunction with estimated tetrode depth. A skull screw was used as a ground while a tetrode left within the corpus callosum picking up minimal neural activity was used as a digital reference and subtracted away from all tetrodes. We let the rat explore an open field with objects and hidden rewards prior to all recording sessions within a sleep box. All experiments were approved by the Rice University Institutional Animal Care and Use Committee’s guidelines and adhered to National Institute of Health guidelines.

2.2. System Framework

Our experimental system architecture, depicted in Figure 1, is a closed-loop system beginning with data acquisition and ending with a digital pulse triggered upon realtime SWR detection. This pulse may be used to trigger a ripple disruption mechanism (e.g., optogenetic fiber or biphasic current stimulator). Data is passed through a headstage to an Open Ephys or SpikeGadgets data acquisition unit, which interfaces with a software suite, Trodes, for which we developed a SWR detection module. Upon detection of a SWR event, the module triggers a stimulation with a digital pulse via an Ethernet-connected BeagleBone Black microcontroller.

2.2.1. Data Acquisition LFP data is collected through tetrodes which connect to a headstage that digitizes the raw analog LFP signal via an onboard analog-to-digital converter. This digitized signal is then transmitted to a computer for display and/or further signal processing. As depicted in Figure 1, step 2, we used two different data acquisition systems, the Open Ephys Acquisition Board and SpikeGadgets Main Control Unit, to acquire the digitized signal at 30 kHz from Intan RHD2000 series headstages. These systems differ in the protocol used to transmit data to the computer—the SpikeGadgets Main Control Unit employs gigabit Ethernet, whereas the Open Ephys

Analysis of an open-source, closed-loop, realtime SWR disruption system

4

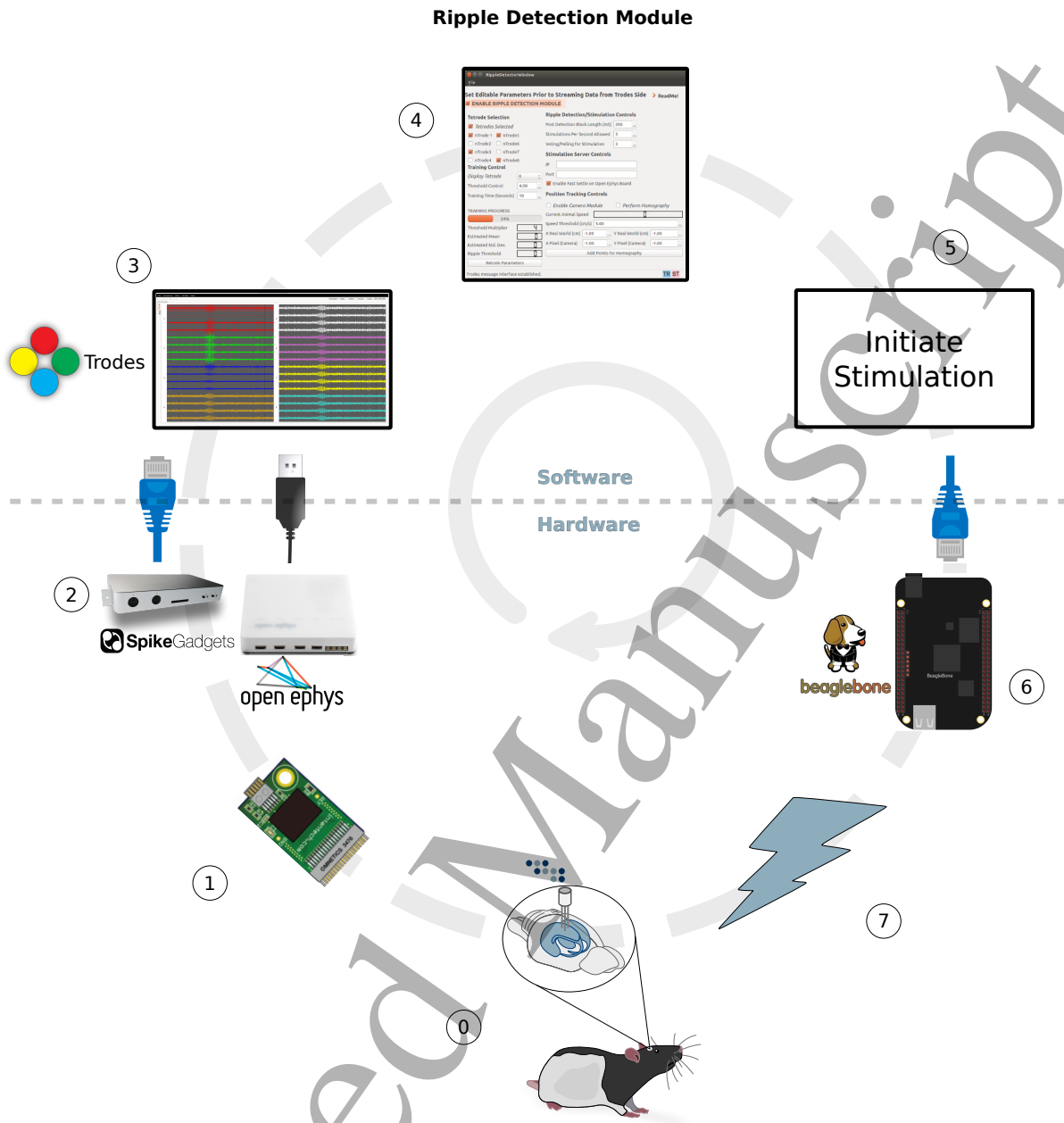
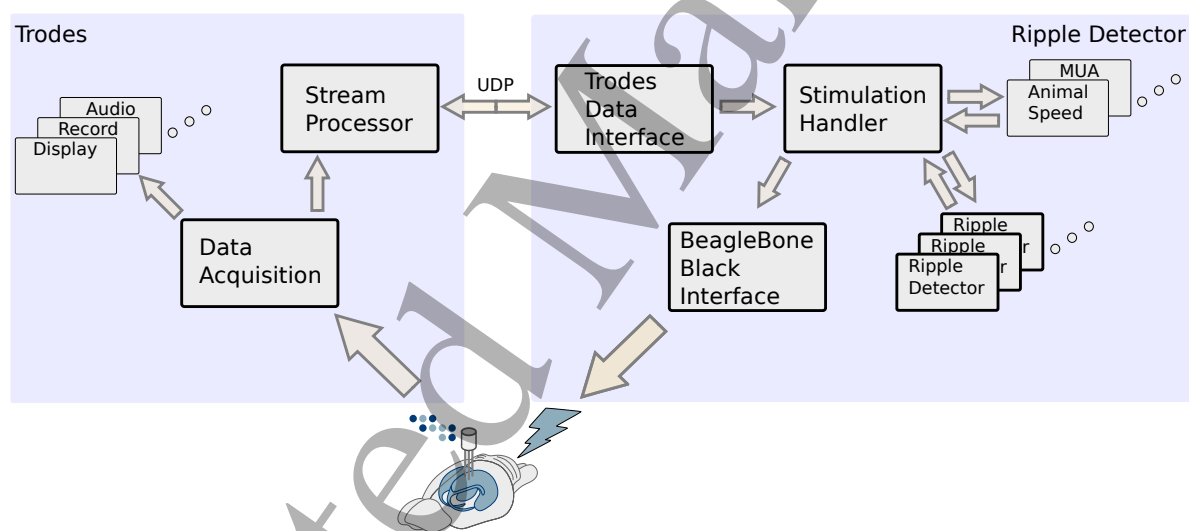


Figure 1: Closed-loop system architecture depicting LFP data acquisition, data transfer (blue Ethernet cables and black USB cable), data processing, and stimulation. Process begins with data acquisition and ends with selective stimulation based on sharp-wave ripple detection. Figure adapted from Open Ephys.

Acquisition Board uses USB2.0. Note that the USB buffer size, is configurable and affects round-trip latency. We found the lowest round-trip latency from 30 kHz data collection to feedback from the BeagleBone Black to be when the number of USB blocks to read was set to three. The two hardware systems evaluated are developed by two organizations, Open Ephys (open-ephys.org) and SpikeGadgets (spikegadgets.com),

2.2.2. Data Processing and Stimulation Trigger Trodes—a modular, open-source, cross platform software suite available from SpikeGadgets (spikegadgets.com/software/trodes.html) for neural data acquisition and interaction and experimental control was used for data collection and signal processing. The software is written in QT/C++ enabling various realtime applications. As depicted on the left side of Figure 2, Trodes is a multi-threaded process with threads interfacing with the data acquisition unit and sending data for realtime display and logging (Figure 1 step 3). Incoming data from both the headstage and available auxiliary channels are sampled at 30 kHz with both acquisition units in this study and handled by the appropriate Trodes Data Acquisition threads. The Stream Processor thread then sends filtered data as requested by connected modules (via UDP in our case). The communication and data transfers are handled via Qthreads and QT signals and slots. This modular framework facilitates custom realtime applications as various forms of data (wide-band electrical signals, spike data, animal position, etc.) can be sent to the module processes using Trodes.



The SWR (or ripple) detection module, user-interface shown in Figure 1 step 4 and block diagram on the right side of Figure 2, receives digitized signals (discussed in the subsection above) of specified channels via UDP communication protocol from the Trodes Stream Processor thread. The digitized signals are sent to the module after a 400 Hz low-pass filter (LFP band) and decimation from 30 kHz to 3 kHz. The

 UNIVERSITY OF NORTH CAROLINA

module process receives the data via the Trodes Data Interface thread and passes it along to a central thread, Stimulation Handler, which spawns off separate threads per channel utilized for ripple detection (algorithm discussed in [Detection Algorithms](#) subsection). Once enough channels report ripple detections within a certain time requirement (15 ms for our experiments) to the Stimulation Handler, a separate thread initiates stimulation by communicating with a BeagleBone Black microcontroller over Ethernet. The microcontroller outputs a 3.3 Volt digital pulse for a user specified amount of time (100 microseconds in this study) to trigger a disruption mechanism for closed-loop intervention. However, as this paper evaluates the efficacy of the detection system, for our analysis we monitor the timestamps at which the disruption pulse is triggered by feeding it into the auxiliary digital inputs of the acquisition units as opposed to stimulation hardware. Lastly, it is worth noting that the ripple detection module user-interface allows users, among other things, to modify parameter and algorithm settings in realtime. More information on the module features and usage, including a tutorial describing the setup process, can be found in the Github link provided in section [2.5](#).

2.3. Detection Algorithms

2.3.1. Canonical Ripple Detection Post-recording, ripple events were defined on tetrodes that displayed characteristics of the CA1 area of the hippocampus. Specifically, the recorded LFP in one of the channels of the selected tetrode (same one subject to online detection for our realtime analysis) first had a digital reference subtracted away. This signal was then LFP band filtered with a 2 tap 400 Hz Bessel low-pass infinite impulse response (IIR) filter (from Trodes). Afterwards the signal was decimated and ripple band filtered with a 25 tap filter (150–250 Hz, FIR bandpass using Hamming window). Ripple band filtering was done using a forward and a time-reversed path, resulting in a net zero group delay (time shift from filtering) and a doubling of the effective filter taps to 50. The instantaneous power of the ripple band filtered signal was then calculated via a Hilbert Transform and further smoothened with a Gaussian kernel with a 4 ms standard deviation. Ripple events were initially detected as times when z-score of the smoothened power signal exceeded a threshold of 3 z-units for at least 15 ms. We further increased the threshold to 4 and 5 z-units while keeping the temporal requirement constant to demonstrate performance on detecting stronger ripples. The canonical ripple epochs were defined as the time points from which the processed signal returned down to the mean before and after threshold crossings [9, 10]. In cases when multiple electrodes (typically channels on different tetrodes) are available for ripple detection, a different canonical definition is required. Ripples were initially defined using as above for each electrode. A canonical multichannel ripple was defined as one which is simultaneously detected on each electrode (two in our analysis). The multichannel ripple epoch is defined as the union of the detected single-channel ripple epochs, i.e., the start of the earliest ripple detected and to end with bound of last ripple

detected. As such, we obtain a conservative ripple detection latency estimate while covering the entire span of the time the LFP is in a high ripple band power state.

2.3.2. Realtime Ripple Detection Like our canonical ripple detections, the realtime or online detection algorithm is comprised of single channel and multichannel modalities. The single channel case performs realtime reference subtraction from the LFP (filtered in the same way as the offline case) and decimation from 30 kHz to 3 kHz as in the canonical detection case. However, the difference between online and canonical detections begins from ripple band filtering. The decimated signal is filtered to the ripple band with a 30 tap FIR filter (150-250 Hz, FIR bandpass using Hamming window). In order to perform a realtime instantaneous power estimation and smoothing, the realtime algorithm computes the absolute value of the ripple band filtered signal and further filters it by a 33 tap 50 Hz low-pass FIR (instead of a Hilbert transform followed by Gaussian kernel smoothing). These filters cause an intrinsic sample delay from the offline case (≈ 10.167 ms in our case). The number of filter taps were chosen to minimize delay for reasonable detection accuracy. To normalize detection thresholds in the realtime case, the mean and standard deviation of the smoothed envelope are estimated over a 20 minute training period. In two ≈ 90 minute sleep box recording sessions, when we sampled 20 minute time intervals at random ($N=1000$), the resulting mean and standard deviation were within 5% of the values for the entire sessions. This length of time and subsequent error in parameter estimation likely depends on the behavioral and/or sleep state of the animal—in our experimental recordings, animals were contained in a sleep box. Realtime detections are then triggered when the envelope crosses a threshold defined as α standard deviations above the mean ($threshold = \alpha * \sigma + \mu$) or α z-units. Following a detection, there is a 200 ms lockout period where the ripple detection module is disabled and does not detect further threshold crossings. This suppresses additional threshold crossings that may be generated from continued rises in ripple band power estimates, stimulation artifacts or excitatory postsynaptic potentials present in LFP. Additionally, we impose a hard limit on the number of detections per second (set to three during the experiments in this work). For multichannel detection, the single channel algorithm runs on separate threads per electrode. A specified number of channels upon which ripples are being detected must all be above threshold within 15 ms of each other in order to trigger a detection event. In the multichannel case, the lockout is imposed following the multichannel detection event. In order to precisely characterize our system, we additionally implemented an offline simulator which carried out the same algorithmic steps in a sample-accurate way. This allowed us to differentiate between algorithmic and hardware, communication, and/or operating system delays.

2.4. Realtime Testing

2.4.1. Synthetic Prior to *in vivo* testing, we developed a synthetic ripple dataset to validate efficacy of our algorithm and to determine baseline latency quantifications. To

replicate CA1 neural noise dynamics within the ripple frequency bands (150–250 Hz), we generated a white noise process and then filtered it to the ripple band. This signal was then adjusted to have the same standard deviation as the ripple band filtered CA1 LFP recording. Ripple events were then injected into the synthetic signal. Synthetic ripples were generated by multiplying a 200 Hz sinusoid with a Gaussian envelope. The envelope was chosen to have ≈ 100 ms standard deviation length (average length of ripple events from our recordings), with a peak value equal to the average maximum peak of ripples found within our recording. This process generated a synthetic ripple event which was then added to the previously generated synthetic neural noise giving us a dataset of synthetic ripples. The final dataset used in our testing was 15 minutes long with 500 injected ripples.

The dataset was then converted to a .wav audio file and played through the realtime system via custom PCB shorting all channels of the headstage to an auxiliary cable input. This framework was used for testing the system with both Open Ephys and SpikeGadgets data acquisition hardware fed into a general purpose computer running Trodes and the ripple detection module on an Ubuntu 14.04 operating system with a quad core Intel Core i7 3.4 GHz processor and 16 GB of RAM. However, different headstages were used for testing these two systems. A 32 channel headstage was used with the Open Ephys hardware while a 128 channel headstage was used with the SpikeGadgets hardware. Digital pulses corresponding to ripple detections, parameter values of the detection algorithm, and wide-band synthetic data across all channels, were logged during each data collection session. It is worth noting that different headstages have inescapable intrinsic noise fluctuations during the recordings. Data was reanalyzed across different channels and using different headstages at different points in time validating our results and subsequent conclusions.

2.4.2. In vivo For *in vivo* testing of our system, a rat was placed inside a sleep box and then tethered to the SpikeGadgets Main Control Unit via a SpikeGadgets HH128 headstage. Data was recorded through our detection module for ≈ 60 -90 minutes in three separate sessions in order to test two different modalities of our algorithm (discussed in [Detection Algorithms](#) subsection) and for synthetic data generation. As in the synthetic case, ripple detection pulses, parameter values of the detection algorithm, and wide-band electrophysiological data across all channels, were logged during each data collection session. Lastly, it is worth noting that prior to the recording sessions, the rat explored an open field with novel objects and hidden rewards in order to increase the prevalence of SWRs [11–15].

2.5. Data Analysis

We characterized system and algorithmic performance via a total of five different metrics: true positive rate (TPR), false discovery rate, false stimulation rate (FSR), detection latency, and relative detection latency. All metrics, other than false discovery

rate, were evaluated on both synthetic and *in vivo* data. Prior to calculating metrics, each ripple event was marked as detected or not detected given an evaluation threshold. Metrics for *in vivo* analyses were generated by first binning the ≈ 80 minute dataset into 15 ms chunks followed by random sampling with replacement of these chunks until a total of ≈ 80 minutes had been sampled. Each 15 ms sample was assigned a flag indicating whether or not it contained a ripple event. If the sample fell within the defined ripple start and end bounds or if the tail end of the time sample contained the start time of a ripple event, the 15 ms sample was considered a ripple sample. True and false positive counts were accumulated based on whether or not the sample contained a ripple event and if the ripple event was marked as detected. The metrics generated were then averaged and this bootstrapping process was repeated 1000 times. Metrics for the synthetic data analysis, however, were calculated over the entire dataset without any bootstrapping or averaging. As we controlled the duration of the synthetic dataset as well as the number of canonical ripples, a false discovery rate metric as opposed to rate was used to characterize performance. Metrics used were calculated as follows:

$$\text{True positive rate, TPR (\%)} = \frac{\text{Number of canonical events detected}}{\text{Number of total canonical events sampled}} * 100$$

$$\text{False discovery rate (\%)} = \frac{\text{Number of false detections}}{\text{Number of total detections}} * 100$$

$$\text{False stimulation rate, FSR (per min)} = \frac{\text{Number of false detections}}{\text{Number of total true negative samples}} * \frac{\text{min}}{\text{sample}}$$

$$\text{Detection latency (ms)} = \text{Ripple detection time} - \text{Canonical ripple onset time}$$

$$\text{Relative detection latency (\%)} = \frac{\text{Detection latency}}{\text{Canonical ripple duration}} * 100$$

In our evaluations of the realtime system, as well as simulated detections, we ignore canonical ripples that had start times within 200 ms of the previous putative ripple since 200 ms is the post disruption lockout period that we use (see Detection Algorithms subsection). All analysis was done with custom Python scripts, a modified version of the nelpy package, and custom C++11 programs. Both analysis code and figure data are publicly available at <https://www.github.com/shayokdutta/RippleDetectionAnalysis>.

3. Results

For closed-loop experiments which seek to disrupt the neural activity that occurs during or in response to SWR, there are three figures of merit: we want to maximize

true positive rate, minimize false stimulation rate and minimize latency. Why are these important? In a closed-loop perturbation experiment, failure to detect a substantial fraction of events will increase the likelihood that no effect of perturbation will be detected. A high rate of false positive-induced perturbations will contaminate experimental results and can potentially cause harm (i.e., seizures). Finally, for most experiments detection latency is just as important as detection accuracy—perturbations that do not perturb the desired patterns while they are going on will not have the intended effect. Using synthetic and actual data, we demonstrate below that these figures of merit are linked and describe their trade-offs for single and multichannel ripple detection.

The SWR detection system we developed and analyzed runs as a module in Trodes (Figure 1, 2). Two features in particular enabled our system analysis: First, as our neural recording system digitizes neural recordings with appropriate anti-aliasing filters, the recorded signal could be converted back to the original analog form modulo a constant scale factor. This enabled us to repeatedly replay identical data into the system to test parameter settings. Second, access to the complete source code—not only of our SWR detection module but also the underlying data acquisition system enabled us to simulate each step of the data processing pipeline. Our module constructs a realtime representation of ripple-band (150–250 Hz) power through a simple FIR filter followed by taking the magnitude of the filtered signal and further smoothing through a low-pass FIR filter (see [Methods](#) and Figure 2). Using statistics of the ripple-power signal learned during an initial training period to normalize, it then detects SWR events as excursions in estimated power over a defined threshold. Note that each of these processing steps deterministically delays the neural signal in ways which depend on the parameters of the algorithm. This work investigates the trade-offs associated with choosing these parameters, particularly the value of the threshold.

We built a detailed simulation of our ripple detection module which carried out the same sample-by-sample computations and produced identical values at each step as the online system. We used synthetic and recorded hippocampal test data to evaluate performance. Using these test data, our algorithm simulation enabled us to quantify how variability in the ripple signal deterministically transformed into variability in detection performance. In parallel, converting the test data back to analog form, we fed them into the actual system and re-digitized the signals including the timestamp of the generated ripple disruption pulse. By comparing the simulated and actual timestamps of ripple detection we could quantify the statistics of the non-deterministic contributors to performance which result from use of a general purpose computer for signal processing. This process enabled us to broadly explore the parameter spaces and extrapolate realtime system performance before actual closed-loop testing *in vivo* (Figure 6).

3.1. Latency and Accuracy trade-offs with Synthetic Data

Variability is one of the greatest challenges in optimizing the detection of particular signals in the brain. In particular, SWR events vary in amplitude, duration, precise frequency content, etc., and while individual large exemplars are easy to identify, even trained investigators have difficulty in determining the boundary between smaller SWR events and spontaneous high frequency oscillations. Thus, in order to confirm the validity of our realtime algorithm, we created a synthetic ripple dataset. This synthetic data was formed by adding 500 ripple events to 15 minutes of background noise. While real ripple events vary in peak amplitude and duration, we used a constant peak amplitude and duration for synthetic ripple events to eliminate the effect of this variation on system performance. This allowed us to analyzed performance as a function of peak amplitude.

Our *in vivo* recording sessions showed a high percentage of ripples with peaks ranging from approximately 5 to 10 z-units in the normalized ripple band power signal. As such, our synthetic ripple library consisted of distinguishable ripples varying in peak size around this range relative to a constant level of background activity (see [Methods](#)). Our module detected ripples both in simulation and via playback to our hardware systems. The detection threshold in the algorithm is specified in terms of z-units—standard deviations above the mean—of the estimated envelope of the underlying synthetic ripple band noise. In the case of large ripples (e.g., Figures 3A and 3B), a detection threshold exists which results in detection of all synthetic ripples and for which incorrect detections (false positives due to background noise) never occur. In the example shown, ripples have a peak power of 10 z-units, and the threshold is set to 5 z-units. When actual events lie closer in power to the background activity, however, it is clear that it will be impossible to select a threshold for which no true events are missed and no false positives are accidentally detected. We quantified this effect by sweeping detection threshold values in datasets generated to contain synthetic ripples with different peak powers.

Across our synthetic datasets, the power of the background noise was held constant. Thus, the false discovery rate depended only on the chosen threshold (Figure 3C). In contrast, detection requires that events be larger than the threshold, yielding a surface where for a given threshold detection accuracy is dependent on ripple amplitude or events will be missed (Figure 3D). Both physiological ripples and our synthetic events have a non-zero rise time. Hence, as the threshold rises, the latency—the delay from when the ripple started (exceeded the mean of the background power) and when it is detected—increases (Figure 3E). Our synthetic ripples were generated using a Gaussian envelope which was scaled by peak power. The result is that larger ripples rise in power faster, and thus are detected with lower latency for a given threshold. As a result, we see that the detection threshold jointly affects latency and accuracy (true and false positive), and thus the optimal setting will depend on the details of a particular experiment.

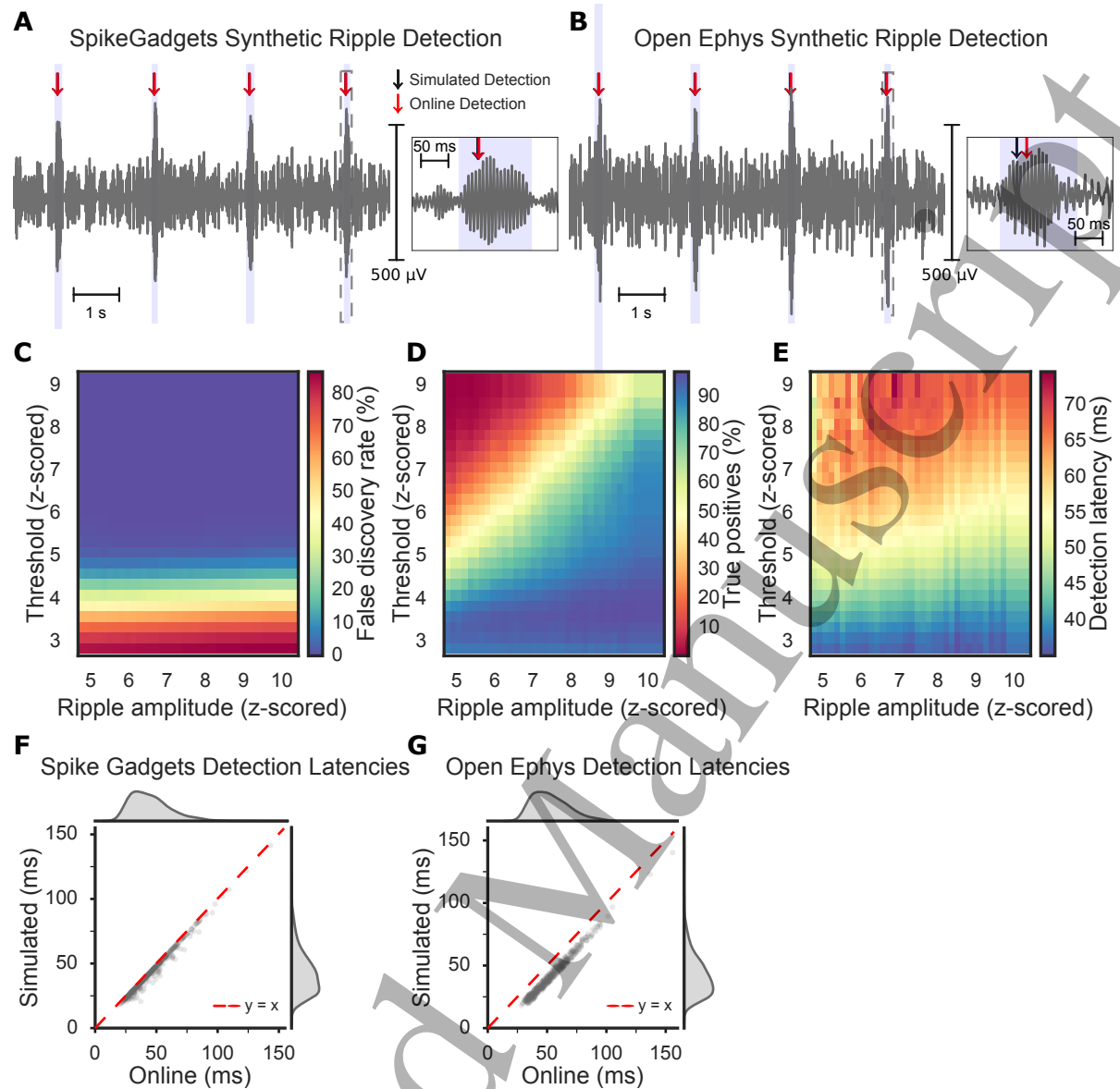


Figure 3: (A, B) Synthetic ripple detection examples with 10 z-unit amplitude ripples using SpikeGadgets and Open Ephys, respectively. Canonical ripples are highlighted and both simulated (black arrow) and online detection (red arrow) times marked. (C–E) Performance characterizations with synthetic ripples of varying amplitudes and simulated online detections with varying thresholds (cooler colors more desirable). (C) False positives reveal threshold at which synthetic ripples exceed baseline noise. (D) True positives taper down with increasing threshold across ripple amplitudes. (E) Average detection latencies show an increasing trend as threshold increases across ripple amplitudes. (F, G) Simulated vs online detection latency scatter plots and distributions for synthetic ripples (from (A,B)) at detection threshold of 5 z-units sent through SpikeGadgets and Open Ephys hardware, respectively. (F) Using SpikeGadgets, average latencies were 42.79 ms and 45.44 ms for simulated and online, respectively, with 80% closed-loop latencies lying within 1.35 and 2.6 ms. (G) Using Open Ephys, average detection latencies were 41.65 ms and 53.32 ms for simulated and online, respectively, with 80% of closed-loop latencies lying within 7.5 and 13.8 ms.

3.2. Realtime Detections with Synthetic Data

Our simulation revealed that choosing a particular value of threshold would yield ripple detections with specific latency and accuracy trade-offs. However, these trade-offs assume that signal processing occurs instantaneously. While some custom-hardware ripple interruption implementations may approach this limit, the need for flexible design has led many investigators to use general purpose computers to carry out computation. In this scenario, communication with hardware and other operating system functions leads to further delay between a ripple occurring and detection yielding a closed-loop response.

In order to quantify these non-algorithmic effects on performance, we proceeded to feed in synthetic data to our realtime system. After estimating a threshold of 5 z-units online by feeding in 2 minutes of background noise, we ran the 15 minute synthetic ripples dataset with 500 injected ripples at 10 z-unit amplitudes. As expected, realtime detections of individual synthetic ripples were identical to our simulations, but with increased latency (deviation from the unity-slope line, Figure 3F and 3G). We found that the additional, realtime latency, was different for our two data acquisition systems (80% of the closed-loop latencies were within 1.35–2.6 ms and 7.5–13.8 ms for SpikeGadgets and OpenEphys, respectively). Given that the system pipeline is identical following data acquisition, this suggests three things. First, in the case of the computations required for ripple detection, time spent computing the algorithm is at most a few milliseconds. Second, the specific interface protocol used for data acquisition, i.e., USB or Ethernet (Figure 1 step number 2), can significantly impact the closed-loop latency. Lastly, this isolates that the majority of overall ripple detection latency lies in the algorithmic implementation—filter-delay and the time it takes for the processed signal to reach threshold—rather than in hardware or computational efficiency. The synthetic analysis as a whole highlighted key performance characteristics of our detection algorithm, validated the efficacy of our realtime system, and identified a speedup with the Ethernet-based SpikeGadgets Main Control Unit—used exclusively for the *in vivo* portion of our study.

3.3. In Vivo Single Channel Detection Analysis

Our investigation of system performance using synthetic data demonstrated that for different amplitude ripples, there would be a trade-off between accuracy and latency. Physiological ripples vary in intensity and duration and the distribution of power in the ripple band is very different than the additive noise assumed in our synthetic analysis. How does this variability affect the performance of a realtime ripple detection system? We began answering this question by applying our system simulation to recorded *in vivo* data. We recorded neural activity from 10 tetrodes implanted in area CA1 of the hippocampus during an ≈ 80 minute session in which a rat rested in a small box. Unlike synthetic data, physiological ripples cannot be identified perfectly. There is no universally agreed definition; we applied three different canonical definitions of ripples

as periods in which the power in the ripple band (150–250 Hz) was elevated above the mean by a threshold (3–5 standard deviations above the mean or z-units) for at least 15 ms. We defined the start and end of each ripple epoch as the moment when the ripple-band power first exceeded and finally returned to the mean (see [Methods](#)). As discussed previously, the detection threshold in our realtime detection algorithm is also specified in terms of z-units of the envelope of the ripple signal. For our *in vivo* parameter explorations, we used mean and standard deviation parameters calculated over the entire 80 minute session.

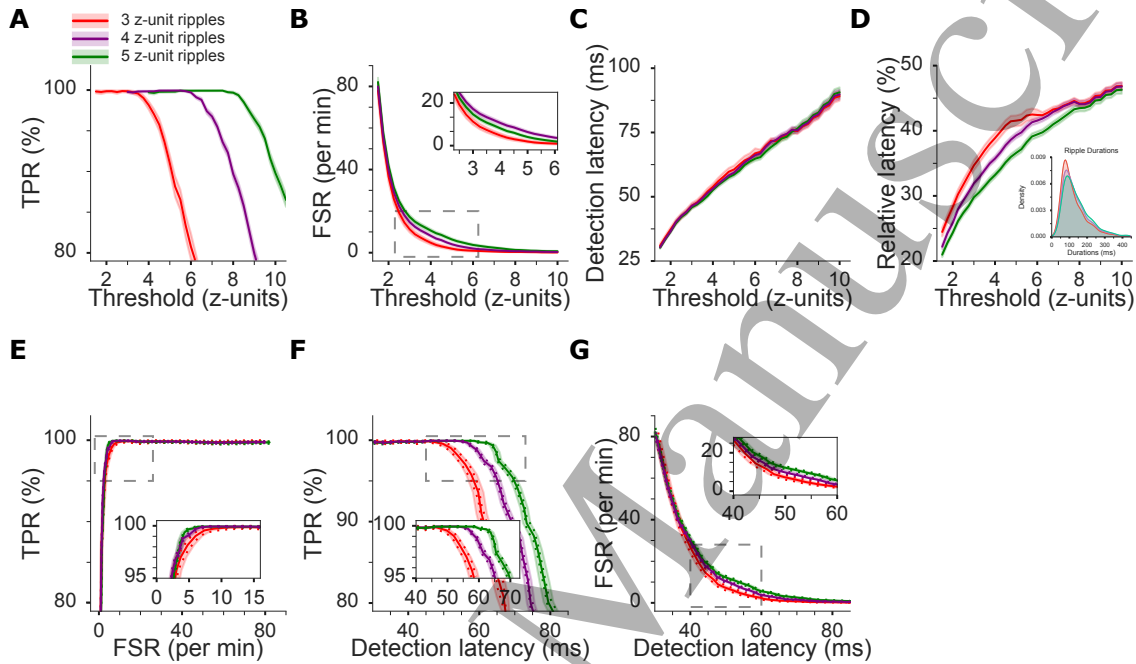


Figure 4: Single channel *in vivo* ripple detection metrics with varying canonical definitions (colored in legend) and varying detection thresholds. Mean and 99% confidence interval of data points (solid and shaded regions, respectively) are shown in (A–D)—generated using a Monte Carlo sampling approach (see [Methods](#)). (A) True rate (TPR) decreases as threshold increases. (B) False stimulation rate (FSR) decreases with increasing threshold. (C) Detection latency increases with increasing threshold. (D) The relative detection latency, the fraction of each event that has transpired prior to detection, also increases with increasing threshold. Inset shows distribution of 98% of ripple durations with 80% of the data falling in between 60 to 150 ms in this dataset. Panels (E–G) show mean and 99% confidence interval of points. The dashed lines represent the confidence interval on the y-axis while the shaded region represents the confidence interval in the x-axis. (E) Receiver operating characteristic (ROC) curve shows true positive and false discovery rate relationships. (F, G) False stimulations decrease with as detection latency increases but true positives also decrease with increasing detection latency.

As with synthetic data, while increasing the threshold parameter, we found that true positives and false positives decreased with increasing detection threshold (Figures 4A–4B). The distribution of ripple-band LFP amplitude is long tailed but falls off

smoothly [10]. Thus, unlike the synthetic case, there are a significant number of “noise” events which only fail to qualify as ripples due to having durations less than 15 ms above the chosen threshold canonical detection. For real data, as we do not know the number of ground truth events, we calculate a false stimulation *rate* to give us an informative characterization of how long we are disrupting information propagation from the hippocampus over a period of time. Note that these rates depend on the canonical definition. We expect the true positive and false positive curves to have the same qualitative shape regardless of the canonical definition. As expected, latency increased with increasing threshold (Figures 4C–4D). Unlike in our synthetic dataset, real ripples vary in duration (inset, Figure 4D). Thus, absolute detection latency does not fully characterize the impact of ripple disruption on downstream regions. To address this, following [8] we calculated a relative latency metric—the percent of the ripple event that has transpired prior to detection (see [Methods](#)). This metric allows us to evaluate what fraction of the average ripple will be transmitted prior to disruption. Over the range of detection thresholds we evaluated, this varied from 20 to 50%, indicating that 50 to 80% of the information transmitted during an average ripple is blocked from being transmitted based on chosen parameters.

We additionally visualized the pairwise trade-off curves relating true positive and false stimulation rates and detection latency (Figures 4E–4G). Unlike with our synthetic data, the false stimulation metric is non-zero for all threshold values (Figure 4B) and there is a larger range for which true positive and false stimulation rates trade off as shown in the receiver operating characteristic (ROC) curve in Figure 4E.

Similar to our synthetic analysis, we explored how our simulated realtime detections would perform on ripples defined by varying power thresholds while keeping the same 15 ms temporal requirement. To do this the threshold of the canonical definition was incremented by one from 3 to 5 z-units. While the curves show the same general trends, this change in the canonical definition enables experimenters to further visualize tradeoffs based on what amplitude of power within the ripple band is believed to represent SWR complexes. Intuitively, Figure 4 shows that as we gear our canonical definition for ripples that maintain higher amplitudes (i.e., more stringent definition), the accuracy curves shift to reflect the increases in false detections and true positives. Although the detection latency curves in Figure 4 are comparable across varying power threshold ripples, the relative latency curves exhibit differences. Specifically, if larger canonical ripples are targeted for disruption (i.e., the green curve), a given threshold yields a lower relative latency than if smaller canonical ripples are targeted. This results from the fact that larger canonical events tend to have longer duration.

Overall, depending on the specifics of experimental design, one can imagine that extraneous perturbations (i.e., false positives) or missed events (i.e., false negatives) might be more detrimental. In many cases, however, investigators would want to pick a threshold value associated with the “elbow” of the ROC (inset in Figure 4E) which is associated with minimizing false positives while maximizing true positives. Our results indicate that when our canonical detection threshold is set to 3 z-units, between 5–

10 false positives detections per minute, greater than $\approx 97\%$ of the canonical ripple events can be detected. The threshold parameter space associated with this region lies in between ≈ 3.5 and 4.25 z-units (Figures 4A and 4B).

3.4. In Vivo Two Channel Detection Analysis

When we examined false positive detections in real data, we noted that a common signature was a brief period of minimally-elevated ripple band power that did not meet the duration criteria. The fact that physiological ripples propagate across CA1 has previously inspired closed-loop ripple detection systems which require a ripple to be detected on multiple electrodes [4, 16]. We implemented and evaluated an algorithm that required that the realtime power estimate be above threshold on two selected channels within 15 ms in order to trigger detection, referred to as the multichannel or two channel algorithm. The canonical ripple definition was updated to use ripples with temporal overlaps across multiple channels (see Methods). For comparison, we analyzed both individual electrodes using the single channel algorithm, but with the new multichannel canonical definition (3 z-unit threshold Figure 5A–5D).

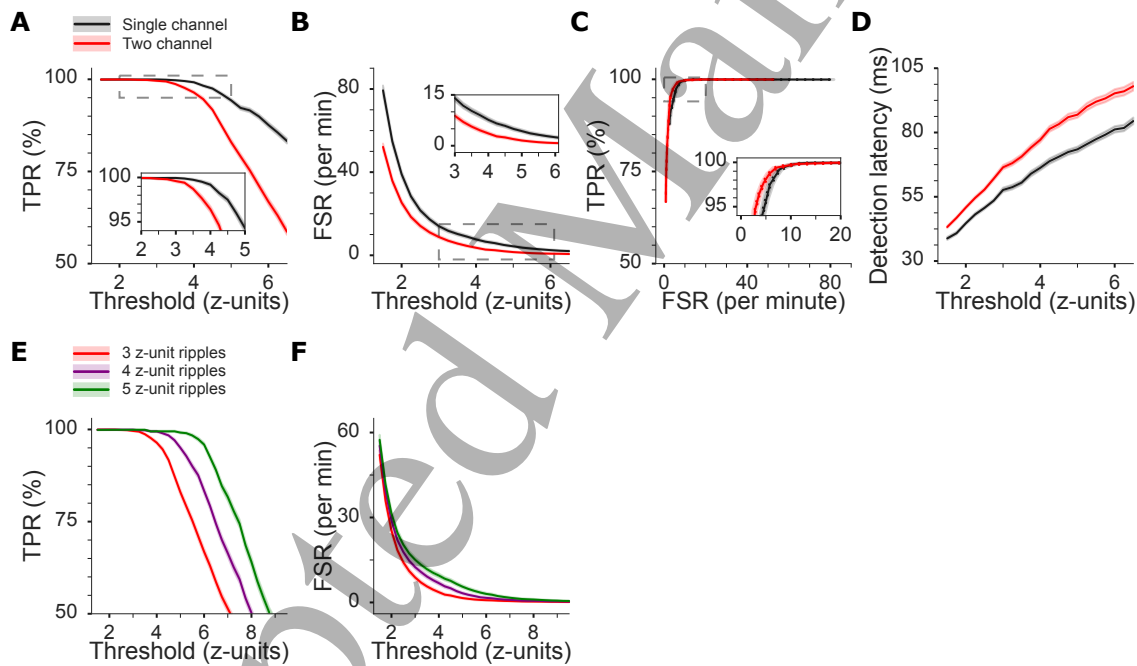


Figure 5: Single channel and two channel in vivo ripple detection metrics. (A–D) Canonical ripple detection threshold set to 3 z-units. Note that two channel detections provide more accurate detection results than single channel at lower thresholds. Threshold/metric definitions and all plots display same metrics and same trends as in Figure 4 but with a two channel comparison and canonical ripples based on two channel detections (see Methods). (E, F) Two channel in vivo canonical ripple detections with varying amplitude threshold requirements.

The more stringent requirement that a ripple be present on multiple channels results in a more rapid decrease in the fraction of true positives detected compared with single channel detection (in which the true multichannel ripple need only be detected on one channel, Figure 5A). As expected, this decreased sensitivity comes with the benefit of increased selectivity (Figure 5B). However, the two channel algorithm can be as sensitive as the single channel algorithm at lower thresholds with lower FPRs. For example, a detection threshold of 3.25 z-units with the two channel voting algorithm results in a higher TPR than single channel detections with a threshold of 4.25 z-units while having comparable average FPRs (insets, Figures 5A and 5B). This is further evinced in the ROC curve which combines true and false positive metrics (Figure 5C).

Intuitively, we expect the two channel algorithm to have higher detection latencies at similar thresholds as it waits for a second channel to detect a ripple prior to triggering a detection pulse. We indeed find this (Figures 5D). Thus, the increased accuracy of multichannel detection comes at the cost of increased latency. As the distribution of ripple durations defined with a 3 z-unit power amplitude threshold lasts on average ≈ 100 ms, the added channel for detection adds up to 15 ms or percent latency. Latency, and the fact that ripples (unlike theta oscillations) are not coherent across the whole hippocampus, suggest that care should be taken in the development of multichannel detection systems [16,17]. Additionally, similar to our single channel analysis we varied our canonical two channel definition threshold from 3 to 5 z-units (Figure 5E and 5F). As with our single channel case, we found increases in both false stimulations and true positives with increased canonical detection threshold amplitudes. Lastly, as the numbers of channels is increased beyond two, our module features a custom-voting algorithm, as opposed to unanimous voting, which requires a user specified voting requirement of ripple detections prior to a stimulation pulse output which may increase sensitivity to investigator preferences [4,18].

3.5. *In Vivo Realtime Detections*

After our offline and simulated analysis, we proceeded to implement the multichannel algorithm in our realtime system. With a rat inside a sleep box for approximately 60 minutes, we ran an *in vivo* two channel voting and detection session. We then set the detection threshold to 3 z-units after estimating mean and standard deviation parameters for 20 minutes (see Methods). According to the two channel analysis, at this threshold we should be able to detect greater than 97% of all ripple events and detection latencies in between 50–55 ms on average. Figure 6A shows a snippet of the recorded LFP and realtime processed signals. Note the temporal lag in the processed signals (see Methods). Two of the single channel ripple detections, traced in dark blue, are not considered part of the canonical ripple epochs, vertically highlighted across all channels. The online detections selectively ignore these events and only detects the canonical ones as they cross threshold across both the channels used for the detection within 15 ms (shown in the bottom realtime envelope traces). Lastly,

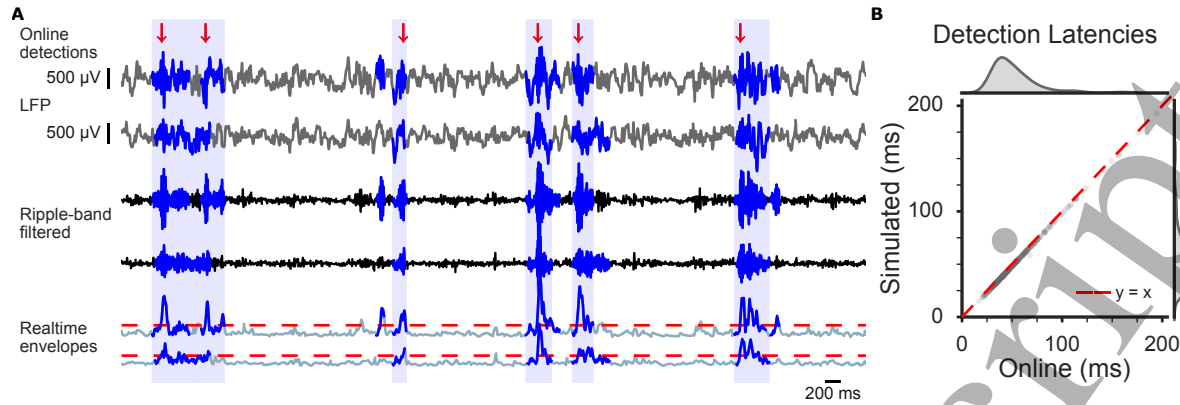


Figure 6: (A) Example snippet of two channel in vivo ripple detections. Blue highlights across all channels mark canonical ripple epochs. Dark blue colored traces in each channel represent individual ripple detections per channel done offline. The red horizontal traces represent realtime threshold of 3 z-units on both channels used for the detection. Realtime traces slightly smoothened for demonstration. Raw traces colored in dark blue. (B) Scatter plot and distributions of detection latencies in between simulated detections (threshold crossing times) and online detections. Average simulated and online detection latencies are 53.322 ms and 54.621 ms, respectively. Average and median latencies between threshold crossing time and online detection time are 1.924 ms and 2 ms, respectively.

as we did while passing our synthetic data through the realtime setup, we examined algorithmic performance in both simulated and online cases. Figure 6B shows the distributions of both online and synthetic detections of the same ripple events during this recording session. We are able to confirm that both our average online and simulated detection latencies, 54.621 ms and 53.322 ms, respectively, fall within the range of our synthetic analysis of this recording session with the given parameters. Additionally, on average the closed-loop latency is ≈ 2 ms indicating that adding another channel is not causing significant computational delay compared to single channel. This was further confirmed by running the online detection algorithm with eight channels voting for ripple detections on our synthetic dataset. We once again found a similar closed-loop latency of approximately 2 ms on average (not shown).

4. Discussion

Within the last decade, electrical and optogenetic ripple disruption studies have established a fundamental role for SWRs in the processes of learning and memory [3–5, 19]. However, performance characterizations of realtime SWR detection systems have not been discussed. Here, we have introduced and evaluated an open-source, closed-loop, realtime system for SWR detection and potential intervention. Our study began with generating a synthetic ripple dataset, revealing subsets of z-scores of ripple band power associated with underlying neural activity and SWRs. We then proceeded to test our algorithm and system performance with the synthetic dataset prior to *in vivo* testing

which motivated further algorithmic improvements and isolated particular pitfalls of our detection algorithm.

For preliminary evaluations of algorithmic performance, we generated a synthetic ripple dataset as ground truth neural data is an underlying challenge in neuroscience. Our online estimated power-threshold crossing algorithm showed that the algorithm was valid in detecting synthetic ripples that were injected into our dataset. However, as mentioned in the [Methods](#) section, the fabrication of the synthetic dataset involved modeling the underlying neural noise within the ripple band. Comparing z-scores of the Hilbert Transform of this signal to the CA1 LFP revealed that the real data encapsulated the modeled noise. We found that the CA1 z-scores that had a longer tail than the modeled noise (z-scores of ≈ 5 and above) were associated with ripple events. As a result, when we injected synthetic ripples into our dataset that had a larger power within the ripple band than the surrounding noise, it was expected that our detection algorithm would be able to selectively detect those events and would be valid criteria for preliminary testing of the realtime system (Figure 3E).

Testing the realtime setup with a synthetic dataset also identified a closed-loop latency speedup by using SpikeGadgets hardware over Open Ephys for data acquisition (Figure 3F–3G). Our results revealed an added latency from simulated to online detections due to computational time and hardware latency. We discovered the latter to be the primary source of the closed-loop latency by demonstrating that adding another thread for detections in our two channel detections (Figure 6B) from our single channel detections (Figure 3F) did not increase the simulated to online detection time latency (the gap from the $y = x$ line). Additionally, we stated the 8 ms speedup by using a SpikeGadgets acquisition unit over the Open Ephys acquisition unit was due to the use of an Ethernet over USB communication protocol. Specifically, the USB protocol involves putting data into packets and then sending those packets with a variable number of blocks of data making up the packets. We varied the number of USB blocks, which increased and decreased the latency, to further confirm that the use of this protocol was the reason for the speedup offered by Open Ephys. The results we presented were found by using the number of USB blocks that provided the lowest latency. It is worth noting that the Open Ephys project is developing a platform for data transfer via PCI express which will enable sub-millisecond closed-loop latency [21]. Lastly, to further confirm that our setup could handle an additional computational load without significantly adding to the detection latency, we tested our realtime system with 8 simultaneous channels detecting synthetic ripples and confirmed that our closed-loop latencies using both systems provided results consistent with single channel detections. This investigation and demonstration further confirmed our claims about the closed-loop latency being a factor of hardware-software interfacing rather than computational time when utilizing 8 total threads. Computational time can potentially become a factor as more threads are added to the detection. In general, we believe that using either data acquisition unit will enable closed-loop ripple disruption experiments as added hardware and computation latencies are $<10\%$ of calculated relative detection latency of ripples.

Moving from synthetic ripple detection to *in vivo* introduced increased false detections due to ripple events sharing ripple band power z-scores with underlying neural activity and noise events from rodent grooming or whisking. Real ripples, unlike our model, do not always reach a value upon which they can be distinctly isolated from other events. This makes the resultant false detections from a single channel threshold crossing algorithm inevitable. In an attempt to lower false detection metrics, we evaluated a multichannel detection algorithm founded on our understanding that ripple events should permeate multiple tetrodes within CA1. Multichannel detections resulted in a lower total number of ripple detections and higher selective detections based on our accuracy metrics than relying upon a single channel (Figure 5). However, unfortunately, both ripple and noise events were coherent across tetrodes. Additionally, events of ripple band power that exceeded threshold without meeting the temporal requirements of our canonical ripples were also prevalent across tetrodes. Using two channels for detections did lower the number of detections due to these neural dynamics but it did not fully address the issue. The remaining challenge involves false detections due to noise events.

As noise events saturate all tetrodes, a proposed solution to handle false detections due to rodent grooming or static passed through to the data acquisition unit would be to utilize a false detection tetrode located in a brain region picking up minimal activity. This false detection channel would perform ripple detections as the previously discussed detection channels but the digital output pulse from our realtime system would be suppressed if this channel reports a detection a few milliseconds before or after (buffer window) the other channel(s) report ripples [22]. Preliminary analysis of this paradigm reveals that false detections due to noise events associated with the reference channel as well as due to rodent grooming or other sources can indeed be suppressed without drastically impacting the true positive rate. However, the trade-off of such an algorithm comes with the extra buffering required after ripple detection. Investigators will have to determine what sort of sensitivity is appropriate given the latency cost of the buffer window.

The other source of false detections, neural dynamics within the LFP associated with ripple band power exceeding thresholds, remains an open question to be solved. Several examples can be found in all of our datasets where ripple band power exceeds thresholds set and triggers our realtime detections but do not meet the 15 ms above threshold temporal requirement of canonical ripples. From the perspective of neural dynamics within the hippocampus, the general purpose of detecting ripples remains to disrupt periods of high multiunit activity co-occurring with important memory processes including sequential reactivation or replay. Absent a gold standard for ripples – an approach for classifying events based on circuit dynamics or functional outcome – the canonical definition may be suspect. If we accept that canonical ripples have some minimum duration, can we add this as a rule to our online system? As previously discussed, we found our relative detection latencies for both modalities of our algorithm to vary between 35%–45% (Figures 4D) at thresholds of interest. Additionally, we found

that $\approx 80\text{--}95\%$ of ripples (depending on the dataset) observed within our study last from $\approx 60\text{--}150$ ms with a mean at ≈ 100 ms. This indicates that every ms of above-threshold temporal requirement added would increase relative detection latency by $\approx 1\%$ of the ripple's duration. Some combination of threshold and online-minimum duration might result in detections that better align with putative ripple events.

The optimal parameter choices in the tradeoff of detection latency and putative accuracy will be determined by the experimental design and the behaviors being studied. One of the putative roles of communication between the hippocampus and the neocortex during ripples is the consolidation of memories [20,23,24]. If fractional ripple disruption results in proportionally-incomplete memory storage, differential effects might be expected for memories which are inherently sequential versus those that are broadly associational. This may potentially explain why ripple disruption during learning of goal-directed behaviors, which might require full sequential reactivation of particular sequences, has been shown to impair performance while disruption during non-sequential tasks (e.g., environmental recognition) tends to have more limited effects [3–6, 19]. Ultimately, further studies and investigations into neural content disrupted upon realtime SWR detection compared to the subset of activity that propagates through to downstream cortical regions are required in order to understand the effects of disruption and purposes served by SWRs.

An important variable in experimental design is whether ripple disruption will take place during resting or during active tasks. Hippocampal recordings in freely behaving animals exhibit increased noise artifacts (i.e., due to cables and environmental inhomogeneities) as well as complex changes in LFP dynamics in the ripple and nearby frequency bands (fast gamma). The latter are particularly pernicious; under the assumption that ripples only occur in non-moving animals, fast-gamma contamination is usually addressed offline using a speed threshold. If we imposed the requirement that canonical ripples could only occur in animals moving less than 5 cm/sec, preliminary simulations indicate that false stimulations would increase from 5-10 per minute in a sleep box to 21 per minute during open field exploration (analyzing data from a 10 minute session using single channel detection with threshold set to 4 z-units). Consequently, while we have not analyzed it in this work, our Trodes module has been upgraded with an interface to a video tracking system which enables speed-thresholds to be imposed online during experiments. As behavioral contexts vary, further investigations into animal speed and awake ripples in the context must be done prior to investigating ripple detection tradeoffs in a behavioral experiment.

5. Conclusion

Altogether, our work investigated the parameter space of ripple detections and identified the trade-offs between true and false positives along with detection latency. Based on the choice of the canonical ripple definition (multichannel in this case) and realtime detection algorithm, it appears that a threshold in the range of 3 to 4 z-

units will enable interaction with $\approx 30\text{-}60\%$ of the ripple event while detecting $\geq 95\%$ of SWRs with < 10 false stimulations per minute for most experiments with a rodent inside a sleep box. The choice of single or multichannel detection will depend on the number of available electrodes and the extent of the perceived importance of detecting coherent events across large fractions of the hippocampus. Our analysis has revealed algorithmic delay is the primary contributor to overall detection latency. In order to interrogate earlier portions of SWRs than the latter 40 to 60 %, which closed-loop ripple disruption systems generally detect, further algorithmic improvement or incorporation of predictive features to SWRs complexes will be required. We anticipate that the low latency, realtime, closed-loop, SWR detection system we implemented in the open-source neural data acquisition software suite, Trodes, may be widely useful, particularly in conjunction with low-cost, open-source data acquisition units from Open Ephys in enabling the dissemination of this experimental technique. With our system, investigators have the ability to further fine-tune the threshold to detect desired events observed online while using our analysis as a guide. Finally, as the number of closed-loop perturbation experiments increases, we hope that our simulation and validation approach will inspire careful exploration of parameter and performance metric spaces.

6. Acknowledgements

This work was supported by National Science Foundation (CBET-1351692 and IOS-1550994), the Human Frontiers Science Program (RGY0088) and the Ken Kennedy Institute for Information Technology. We are grateful for the assistance of past and present Realtime Neural Engineering lab members during data acquisition. Additionally, we would like to thank Chun-Ting Wu, Matthijs van der Meer and members of the van der Meer lab for beta testing our realtime SWR detection system.

References

- [1] Clark R E, Zola S M and Squire L R 2000 Impaired recognition memory in rats after damage to the hippocampus *J. Neurosci.* 20 885360
- [2] Maren S, Aharonov G and Fanselow M S 1997 Neurotoxic lesions of the dorsal hippocampus and Pavlovian fear conditioning in rats *Behav. Brain Res.* 88 26174
- [3] Girardeau G, Benchenane K, Wiener S I, Buzsáki G and Zugaro M B 2009 Selective suppression of hippocampal ripples impairs spatial memory *Nat. Neurosci.* 12 12223
- [4] Jadhav S P, Kemere C, German P W and Frank L M 2012 Awake hippocampal sharp-wave ripples support spatial memory *Science* 336 14548
- [5] Ego-Stengel V and Wilson M A 2010 Disruption of ripple-associated hippocampal activity during rest impairs spatial learning in the rat *Hippocampus* 20 110
- [6] Kovács K A, O'Neill J, Schoenenberger P, Penttonen M, Ranguel Guerrero D K and Csicsvari J 2016 Optogenetically Blocking Sharp Wave Ripple Events in Sleep Does Not Interfere with the Formation of Stable Spatial Representation in the CA1 Area of the Hippocampus *PLoS One* 11 e0164675

- [7] Novitskaya Y, Sara S J, Logothetis N K and Eschenko O 2016 Ripple-triggered stimulation of the locus coeruleus during post-learning sleep disrupts ripple/spindle coupling and impairs memory consolidation *Learn. Mem.* 23 23848
- [8] Ciliberti D and Kloosterman F 2017 Falcon: a highly flexible open-source software for closed-loop neuroscience J. Neural Eng. 14 045004
- [9] Cheng S and Frank L M 2008 New Experiences Enhance Coordinated Neural Activity in the Hippocampus *Neuron* 57 30313
- [10] Kemere C, Carr M F, Karlsson M P and Frank L M 2013 Rapid and continuous modulation of hippocampal network state during exploration of new places *PLoS One* 8 e73114
- [11] Wilson M and McNaughton B 1994 Reactivation of hippocampal ensemble memories during sleep *Science* 265 6769
- [12] O'Neill J, Senior T J, Allen K, Huxter J R and Csicsvari J 2008 Reactivation of experience-dependent cell assembly patterns in the hippocampus *Nat. Neurosci.* 11 20915
- [13] Buzsáki G 2015 Hippocampal sharp wave-ripple: A cognitive biomarker for episodic memory and planning *Hippocampus* 25 1073188
- [14] Girardeau G, Cei A and Zugaro M 2014 Learning-induced plasticity regulates hippocampal sharp wave-ripple drive J. Neurosci. 34 517683
- [15] Singer A C and Frank L M 2009 Rewarded outcomes enhance reactivation of experience in the hippocampus *Neuron* 64 91021
- [16] Patel J, Fujisawa S, Berényi A, Royer S and Buzsáki G 2012 Traveling theta waves along the entire septotemporal axis of the hippocampus *Neuron* 75 4107
- [17] Patel J, Schomburg E W, Berényi A, Fujisawa S and Buzsáki G 2013 Local generation and propagation of ripples along the septotemporal axis of the hippocampus *J. Neurosci.* 33 1702941
- [18] Yu J Y, Kay K, Liu D F, Grossrubatscher I, Loback A, Sosa M, Chung J E, Karlsson M P, Larkin M C and Frank L M 2017 Distinct hippocampal-cortical memory representations for experiences associated with movement versus immobility *Elife* 6
- [19] van de Ven G M, Trouche S, McNamara C G, Allen K and Dupret D 2016 Hippocampal Offline Reactivation Consolidates Recently Formed Cell Assembly Patterns during Sharp Wave-Ripples *Neuron* 92 96874
- [20] Bontempi B, Laurent-Demir C, Destrade C and Jaffard R 1999 Time-dependent reorganization of brain circuitry underlying long-term memory storage *Nature* 400 6715
- [21] Newman, J P, *et al.* 2017 An open-source PCIe based electrophysiology system for high data rate, low-latency closed-loop experiments *Program No: 528.06 Neuroscience Meeting Planner* (Washington DC: Society for Neuroscience) (online)
- [22] Girardeau G, Inema I and Buzsáki G 2017 Reactivations of emotional memory in the hippocampus-amygdala system during sleep *Nat. Neurosci.* 20 163442
- [23] Eichenbaum H 2000 A cortical-hippocampal system for declarative memory *Nat. Rev. Neurosci.* 1 4150
- [24] Maviel T, Durkin T P, Menzaghi F and Bontempi B 2004 Sites of neocortical reorganization critical for remote spatial memory *Science* 305 969